

IGR J12580+0134: A Candidate for Repeating Partial Tidal Disruption Events Supported by Multi-Wavelength Observations

PO MA ¹, SHAO-YU FU ¹, LINHUI WU ², WEI-HUA LEI ¹ AND QIANG YUAN ^{3,4}

¹Department of Astronomy, School of Physics, Huazhong University of Science and Technology, Luoyu Road 1037, Wuhan, 430074, China

²Shanghai Astronomical Observatory, Chinese Academy of Sciences, 80 Nandan Road, Shanghai, 200030, P. R. China

³Key Laboratory of Dark Matter and Space Astronomy, Purple Mountain Observatory, Chinese Academy of Sciences, Nanjing 210023, China

⁴School of Astronomy and Space Science, University of Science and Technology of China, Hefei 230026, China

ABSTRACT

Repeating partial tidal disruption events (pTDEs) provide a direct probe of stellar orbits and episodic mass loss around supermassive black holes, but robust identification requires multi-band and multi-epoch evidence. We investigate whether the late-time radio rebrightening of the nuclear transient IGR J12580+0134 in NGC 4845 can be explained as a repeating pTDE, using multi-epoch Karl G. Jansky VLA observations together with X-ray constraints from *Swift*/XRT and *NICER*. The radio light curves show two distinct episodes, with the L-band peaks separated by ≈ 1513 days. Modeling the second episode with a synchrotron afterglow framework using Markov Chain Monte Carlo fitting favors a non-relativistic outflow $v \simeq 0.03c$, with an isotropic-equivalent kinetic energy of order 10^{50} erg propagating in an approximately constant-density circumnuclear medium. No significant contemporaneous brightening is detected by *Swift*/XRT during the 2016 radio flare, while faint *NICER* flares in 2023 suggest intermittent low-level accretion. The recurrence timescale and radio energetics therefore make IGR J12580+0134 a possible candidate for a repeating pTDE system, motivating continued sensitive radio and X-ray monitoring to test future reactivations.

Keywords: Tidal disruption (1696);

1. INTRODUCTION

When a star approaches the tidal radius of a supermassive black hole (SMBH), it can be fully disrupted by tidal forces. A fraction of the stellar debris is subsequently bound and falls back, producing a luminous flare whose bolometric luminosity and decline rate encode the nature of the disrupted body and the efficiency of circularisation (M. J. Rees 1988). Such events, called tidal disruption events (TDEs), provide a unique method to study accretion and jet-launching physics around SMBHs of quiescent galaxies (Y. Wang et al. 2025).

A tidal encounter does not necessarily lead to a full disruption. If the stellar pericentre is sufficiently large, the star can survive the passage and lose only a fraction of its mass, resulting in a similar flare. In this case, a partial tidal disruption event (pTDE) happens (T. Wevers et al. 2023; J. J. Somalwar et al. 2025; J. Guillochon

& E. Ramirez-Ruiz 2013; E. R. Coughlin & C. J. Nixon 2019). The encounter strength is commonly quantified by the penetration factor, $\beta \equiv R_t/R_p$, where R_p is the pericentre distance. In recent years, numerical simulations have shown that the critical β values separating the onset of partial disruption from full disruption depend sensitively on the internal structure of the star (e.g., J. Guillochon & E. Ramirez-Ruiz 2013; T. Ryu et al. 2020a). Several theoretical studies suggest that partial disruptions may occur at rates similar to, or exceeding, those of full disruptions, implying that pTDEs could make an important contribution to the total TDE population (e.g., N. C. Stone & B. D. Metzger 2016; T. Ryu et al. 2020b; N. C. Stone et al. 2020; J.-H. Chen & R.-F. Shen 2021; S. Zhong et al. 2022). Moreover, numerical simulations predict that pTDEs can exhibit fallback-rate evolutions distinct from those of full disruptions, potentially imprinting observable differences on the light-curve decline. For full disruptions, the fallback rate is expected to approach the canonical late-time decay, $\dot{M}_{\text{fb}} \propto t^{-5/3}$ (M. J. Rees 1988; E. Phinney

1989), in contrast, numerical simulations suggest that partial disruptions can exhibit steeper fallback decays, approaching $\dot{M}_{\text{fb}} \propto t^{-9/4}$ in certain regimes (J. Guillochon & E. Ramirez-Ruiz 2013; E. R. Coughlin & C. J. Nixon 2019; T. Ryu et al. 2020a).

While the fallback-rate evolution may provide a useful diagnostic, it can be challenging to identify pTDEs from a single flare alone. A more distinctive signature is offered by systems that produce multiple episodes of nuclear flaring. Such repeated pTDEs can arise when a star is placed on a bound, highly eccentric orbit around an SMBH and undergoes partial stripping at successive pericentre passages (R.-F. Shen 2019; J.-H. Chen et al. 2023; D. Li et al. 2025). One possible formation channel is the Hills mechanism, in which a stellar binary is tidally separated during a close passage by the SMBH, ejecting one component as a hypervelocity star while capturing the other onto a tight orbit (J. G. Hills 1988). The captured star may then experience repeated partial disruptions as it returns to pericentre, producing a sequence of flares separated by months to years (M. Cufari et al. 2022; W. Lu & E. Quataert 2023). Such repeated events offer a direct observational pathway to establishing partial disruptions, since recurrence naturally follows from the survival of the star after the initial passage.

Observationally, repeated pTDE candidates are typically characterised by multi-episode nuclear flaring activity with recurring timescales, often accompanied by similarities in photometric and spectroscopic properties between episodes. Nevertheless, confirming repeated pTDEs can be non-trivial, since alternative scenarios—such as double TDEs from stellar binaries, SMBH binaries, or enhanced nuclear transient rates in dense stellar environments—may also produce multi-episode flaring behaviour (e.g., I. Mandel & Y. Levin 2015; X.-J. Wu & Y.-F. Yuan 2018; I. Arcavi et al. 2014; E. Hammerstein et al. 2023; M. Wang et al. 2024; H. Pfister et al. 2020).

To date, only a small number of repeated pTDE candidates have been reported in the literature. These sources are characterised by multi-episode nuclear flares recurring on timescales from days to years, and some exhibit similar photometric and/or spectroscopic properties across different episodes. We summarise their basic observational properties in Table 1. The diversity of recurrence timescales and multi-wavelength behaviours among these candidates highlights the need for further theoretical work.

IGR J12580+0134 is a TDE that occurred in 2011 in the nucleus of the nearby galaxy NGC 4845 with a redshift distance of 18 Mpc (R. Walter et al. 2011; W.-H. Lei et al. 2016; Q. Yuan et al. 2016; N. Yu et al.

2022). Discovered by *INTEGRAL*, the event exhibited a sub-Eddington X-ray flare consistent with the tidal disruption of a super-Jupiter-mass object (R. Walter et al. 2011; M. Niłkołajuk & R. Walter 2013). A compact radio counterpart was detected later that year, showing rapid brightening and subsequent evolution consistent with synchrotron emission from an expanding outflow (J. A. Irwin et al. 2015; E. S. Perlman et al. 2017).

A late-time radio-only flare was reported more than a decade after the original event (E. S. Perlman et al. 2022). This rebrightening was interpreted as resulting from the interaction between the initial outflow and dense circumnuclear material (E. S. Perlman et al. 2017, 2022). Here, we argue that the recurrence timescale and energetics are instead more naturally explained by a repeated partial tidal disruption event (pTDE), identifying IGR J12580+0134 as a candidate for a recurring TDE system.

This paper is organized as follows. Section 2 describes the observational data and data reduction procedures. In Section 3, we present the theoretical framework for the repeating tidal disruption scenario. Section 4 provides the main results, where the physical parameters of the outflow are constrained from radio observations using Markov Chain Monte Carlo (MCMC) methods. Finally, Section 5 summarizes our findings and discusses their implications for interpreting IGR J12580+0134 as a candidate repeating partial tidal disruption event.

2. OBSERVATIONS AND DATA REDUCTION

2.1. Radio Data

We make use of archival radio data from IGR J12580+0134 from E. S. Perlman et al. (2022), who compiled a comprehensive data set of flux density measurements spanning from 1995 to 2019, based on Karl G. Jansky Very Large Array (VLA) observations across the L, C, S, and X bands. These include archival observations obtained before TDE, as well as VLA data taken during the TDE epoch in 2011–2012 as part of the CHANG-ES project (PI: J. Irwin; observation code: 10C-119; J. A. Irwin et al. 2012). These observations cover L-band and C-band frequencies (centered at 1.6 and 6.0 GHz, respectively) and were conducted in three different array configurations: B, C, and D. In 2015, the source was also observed in the L and C bands as part of the VLA project 15A-357 (PI: E. Meyer). Data reduction and imaging details are described in J. A. Irwin et al. (2012) and T. Wiegert et al. (2015).

In the NRAO data archive, we identified two additional VLA observations that include IGR J12580+0134. The observation project codes are 21A-033 (PI: Yelena Stein) and 22B-016 (PI is also

Yelena Stein). The advent of the *Very Large Array Sky Survey* (VLASS) — currently the most sensitive, wide-area radio survey of the northern sky — offers a powerful new avenue for identifying late-time, rising radio emission from previously known TDE candidates. VLASS commenced on 2017 September 7 and employs the VLA to map approximately 80% of the radio sky over three sequential epochs spanning seven years (M. Lacy et al. 2020). All observations are conducted in the S band (2–4 GHz), achieving a typical single-epoch rms sensitivity of $\sim 100 \mu\text{Jy}$, sufficient to detect radio outflows comparable to those observed in known TDEs. We also extracted radio images of IGR J12580+0134 from the VLASS, specifically from the Quick Look images of VLASS Epoch 3.2.

We briefly summarize the VLA data reduction procedure in the following. All newly presented observations (project codes: 21A-033 and 22B-016) were reduced using the Common Astronomy Software Applications package (CASA; J. P. McMullin et al. 2007) following standard calibration protocols (see, e.g., J. Irwin et al. 2013; T. Wiegert et al. 2015).

Flux density and bandpass calibration were conducted using 3C286, while J1224 + 0330 was used to calibrate the time-variable complex gains. As a well-known standard calibrator, 3C286 provides stable flux densities across a wide frequency range and is commonly adopted in VLA observations (R. A. Perley & B. J. Butler 2013). We note that bad data and RFI flagging are conducted throughout the entire calibration process with CASA task FLAGDATA.

Total intensity images were produced for each observation using the CLEAN task in CASA. The uv data were Fourier transformed into the image plane to create a dirty map, and the corresponding point spread function (PSF, or "dirty beam") was deconvolved using the CLEAN algorithm (B. Clark 1980). We employed the multi-scale multi-frequency synthesis (MS-MFS) mode (U. Rau & T. J. Cornwell 2011) to better recover extended and faint emission, and adopted a Briggs weighting scheme with a robust parameter of 0 (or 0.5) to balance resolution and sensitivity.

Disk emission has been estimated to be 7 ± 1 mJy in the C band and 19 ± 4 mJy in the L band (J. A. Irwin et al. 2015). Assuming a spectral index of -0.74 for the disk emission, the interpolated flux density at the S band is calculated to be approximately 11.8 mJy. For the S-band data presented in this work, we have subtracted the estimated contribution from the host galaxy disk emission to isolate the flux density of the AGN component. Radio observations are shown in Table 2

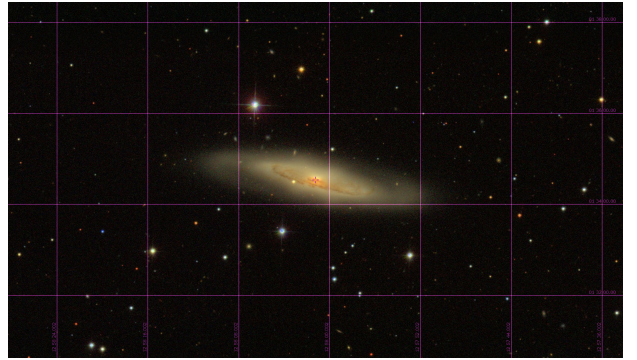


Figure 1. SDSS image showing the location of NGC 4845 at RA = $12^{\text{h}}58^{\text{m}}01^{\text{s}}$, Dec = $+01^{\circ}34'33''$. The image was obtained from the SDSS SkyServer Navigate tool (<https://skyserver.sdss.org/dr18/VisualTools/navi2>).

2.2. X-ray Data

IGR J12580+0134 was first identified as a luminous X-ray flare in the nucleus of NGC 4845, consistent with a TDE. The event was traced by follow-up *XMM-Newton* observations in January 2011 and is widely interpreted as the disruption of a substellar object by a low-mass supermassive black hole (M. Nikolaĵuk & R. Walter 2013).

Spectral analyses of the 2011 observations reveal a heavily absorbed power-law continuum with photon index $\Gamma \approx 2.2$ and hydrogen column density $N_{\text{H}} \sim 7 \times 10^{22} \text{ cm}^{-2}$, characteristic of an accreting source. The average 2–10 keV flux reached $\sim 6 \times 10^{-11} \text{ erg cm}^{-2} \text{ s}^{-1}$, confirming the extreme luminosity of the flare (M. Nikolaĵuk & R. Walter 2013). Moreover, the X-ray light curve follows the canonical $t^{-5/3}$ decline expected from fallback accretion after tidal disruption, providing strong support for the TDE interpretation (M. J. Rees 1988).

Despite continued multiwavelength monitoring, E. S. Perlman et al. (2022) analyzed new late-time *Swift*/XRT observations obtained during the 2016 radio flare, together with archival *Swift* and *XMM-Newton* data from M. Nikolaĵuk & R. Walter (2013). They reported no statistically significant X-ray brightening during the 2016 radio flare. Because the individual observations had limited counts, E. S. Perlman et al. (2022) co-added the final three *Swift* datasets to improve the signal-to-noise ratio, producing a single flux measurement that we adopt and display in Figure 2.

More recently, Neutron star Interior Composition Explorer (hereafter *NICER*) monitoring has revealed faint X-ray flares during March–June 2023 that are substantially weaker than the 2011 outburst. These low-luminosity events are likely associated with extremely weak accretion onto the central black hole and may indicate the presence of a low-luminosity active galactic nu-

cleus (A. Danehkar 2025). We also adopt these *NICER* measurements and display them in Figure 2.

3. MODELING

3.1. The Possibly Orbital Period of IGR J12580+0134

For IGR J12580+0134, we estimate the orbital period by adopting the time separation between the radio L-band peaks of the first and second flares. However, strictly speaking, the observed peak separation does not equal the true orbital period. Instead, it obeys

$$\Delta T_{\text{obs}} = T_{\text{orb}} - T_{\text{peak},1} + T_{\text{peak},2}, \quad (1)$$

where ΔT_{obs} is the observed separation between the two peaks in the L band (2012-Mar-30 and 2016-May-21), T_{orb} is the orbital period, and $T_{\text{peak},1}$ and $T_{\text{peak},2}$ denote the delays to the peak fallback rate following the first and second passages, respectively. The two peak times, $T_{\text{peak},1}$ and $T_{\text{peak},2}$, will generally not be identical, since the surviving stellar core is spun up during each passage (T. Ryu et al. 2020b; A. Bandopadhyay et al. 2024) and simultaneously loses mass as a result of partial disruption. Here we assume that the peak luminosity traces the peak fallback rate. According to Table 2, $\Delta T_{\text{obs}} \approx \Delta T = 1513$ days.

For a black hole with mass $M_{\text{BH}} \approx 3 \times 10^5 - 1.8 \times 10^7 M_{\odot}$ (W.-H. Lei et al. 2016), an orbital period of 1513 days corresponds to a semi-major axis of $a \sim (2.58 \times 10^{15} - 1.01 \times 10^{16})$ cm. Using the stellar velocity dispersion (σ) of NGC 4845 obtained from the HyperLeda¹ database (D. Makarov et al. 2014), we estimate the radius of influence of the SMBH as

$$r_{\text{infl}} \simeq \frac{GM_{\text{BH}}}{\sigma^2} \approx (2.22 \times 10^{17} - 1.33 \times 10^{19}) \text{ cm}, \quad (2)$$

which is larger than the derived semi-major axis a by one to two orders of magnitude.

Since most disrupted stars originate in this region, tidal dissipation alone is insufficient to bind the star tightly enough to yield an orbital period of 1500 days (M. Cufari et al. 2022). A plausible dynamical pathway is the Hills mechanism (J. G. Hills 1988). In this process, the center of mass of a binary star with total mass M_b and separation a_b approaches the SMBH on an orbit with a pericenter distance smaller than $R_a = a_b(M_{\text{BH}}/M_b)^{1/3}$, at which the binary is tidally disrupted. One star is ejected from the system, whereas the companion becomes bound to the SMBH with an orbital period of order of years.

For mass transfer or partial disruption to occur, the pericenter distance must be comparable to the tidal

radius. This corresponds to a penetration factor of $\beta \equiv R_t/R_p \gtrsim 0.6$ (i.e., $R_p \lesssim 2R_t$), such that the star begins to lose mass once it passes within approximately twice the tidal radius (E. R. Coughlin & C. J. Nixon 2022).

Furthermore, the orbital period of the captured star can be estimated from the binding energy imparted during the tidal breakup of the binary. The typical period scales as

$$T_* \sim \frac{a_b^{3/2}}{\sqrt{GM_b}} \left(\frac{M_{\text{BH}}}{M_b} \right)^{1/2}. \quad (3)$$

To avoid disruption before reaching R_t , the binary separation must satisfy (G. D. Quinlan 1996),

$$a_b \lesssim \frac{GM_b}{\sigma^2}. \quad (4)$$

Combining these expressions yields

$$T_* \lesssim \frac{GM_b}{\sigma^3} \left(\frac{M_{\text{BH}}}{M_b} \right)^{1/2}. \quad (5)$$

According to $M_{\text{BH}}-\sigma$ relation (K. Gebhardt et al. 2000; L. Ferrarese & D. Merritt 2000), the above constraint becomes

$$T_* \lesssim 1721 \left(\frac{M_b}{M_{\odot}} \right)^{1/2} \left(\frac{M_{\text{BH}}}{M_0} \right)^{-47/506} \text{ days}, \quad (6)$$

here we adopt $M_0 = 1.17 \times 10^8 M_{\odot}$, $\sigma_0 = 200 \text{ km s}^{-1}$, and $n = 5.06$ (N. J. McConnell & C.-P. Ma 2013), because NGC 4845 belongs to late-type galaxies. This suggests that orbital periods of several thousand days are plausible for typical parameters, consistent with the ~ 1500 days period inferred for IGR J12580+0134.

Thus, the Hills mechanism provides a natural explanation for capturing the star onto such a tight orbit, making subsequent partial tidal disruptions possible.

In order to constrain the orbital parameters of the bound star, we follow the analytical framework developed in the context of AT2022dbl (L. Makrygianni et al. 2025). In that work, the authors employed the Hills mechanism together with angular momentum relaxation to derive the eccentricity constraint for stars captured by a SMBH. Building upon this formulation, we apply the same relation to our system and carry out explicit estimates in order to verify the consistency between theoretical expectations and the observed orbital period.

¹ <http://leda.univ-lyon1.fr/>

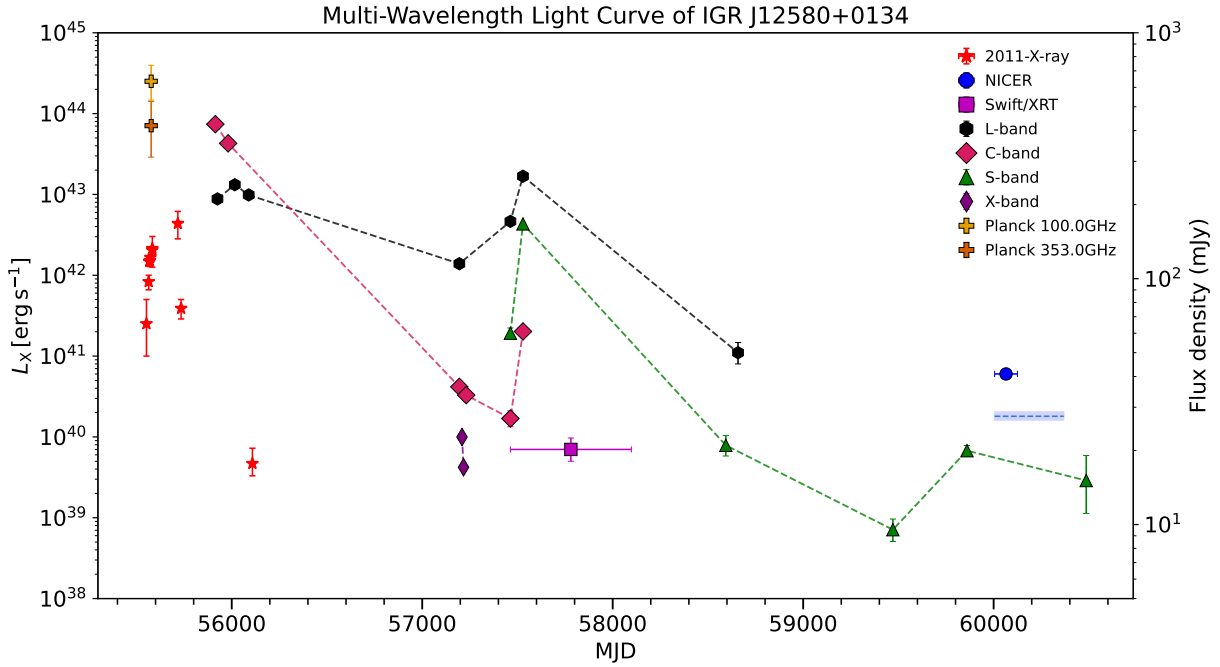


Figure 2. Multi-wavelength light curves of IGR J12580+0134, combining X-ray and radio data. Radio fluxes are plotted for L-band (black hexagons), C-band (pink diamonds), S-band (green triangles), and X-band (purple thin diamonds). Red stars represent the 2011 X-ray flare in the 17.3–80 keV band (data from M. Nikolajuk & R. Walter 2013). The Swift/XRT observation (0.5–7 keV) is shown as magenta squares. A faint X-ray flare detected in 2023 via NICER (0.4–10 keV) monitoring is indicated by blue circles and the shaded region indicating the background flux level between 2021 June 15 and 2024 February 28 (data from A. Danehkar 2025). Early submillimeter measurements from Planck at 100 and 353 GHz are shown as golden pentagons and dark-orange crosses (data from Q. Yuan et al. 2016). The fluxes are plotted on a logarithmic scale to highlight the dynamic range of the event.

Specifically, the orbital eccentricity can be expressed as

$$\begin{aligned}
 1 - e & \\
 & \approx \beta_*^{-1} (2\pi)^{2/3} \frac{R_*}{(GM_* T_*^2)^{1/3}} \\
 & \approx 0.0026 \left(\frac{T_*}{1500 \text{ d}} \right)^{-3/2} \left(\frac{R_*}{R_\odot} \right) \left(\frac{M_*}{M_\odot} \right)^{-1/3} \left(\frac{\beta_*}{0.7} \right)^{-1}.
 \end{aligned} \tag{7}$$

where $\beta_* = R_t/R_p$ is the penetration factor, R_* and M_* are the stellar radius and mass, T_* is the orbital period. In our analysis, we adopt $\beta_* = 0.7$. For a solar-type star ($M_* = 1M_\odot$, $R_* = 1R_\odot$) around a black hole of $M_{\text{BH}} \sim 10^6 M_\odot$ with $\beta_* = 0.7$, we obtain an eccentricity $e \approx 0.9974$ and $R_p \approx 10^{13}$ cm. This corresponds to a semi-major axis of $a \approx R_p/(1 - e) \approx 3.85 \times 10^{15}$ cm.

3.2. Estimating the Disrupted Mass at the Second Encounter

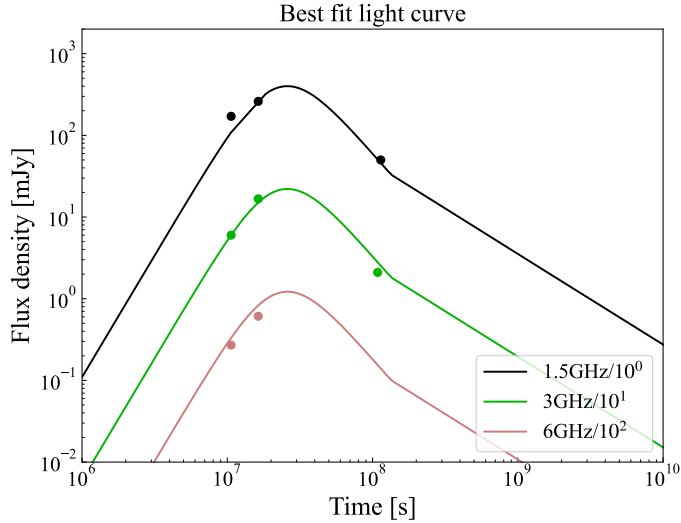
We adopt the isotropic-equivalent kinetic energy constrained by our radio afterglow modeling, which corresponds to $E_{\text{iso}} \simeq 2.99 \times 10^{50}$ erg.

If we assume a non-relativistic outflow with a characteristic velocity $v = 0.03c$ (as fixed in our MCMC analysis), the total kinetic energy of the outflow satisfies $E_{\text{true}} \simeq 0.5M_{\text{out}}v^2 \sim E_{\text{iso}}$, where M_{out} denotes the total mass participating in the outflow on both sides. Solving the expression for M_{out} results in $0.186 M_\odot$.

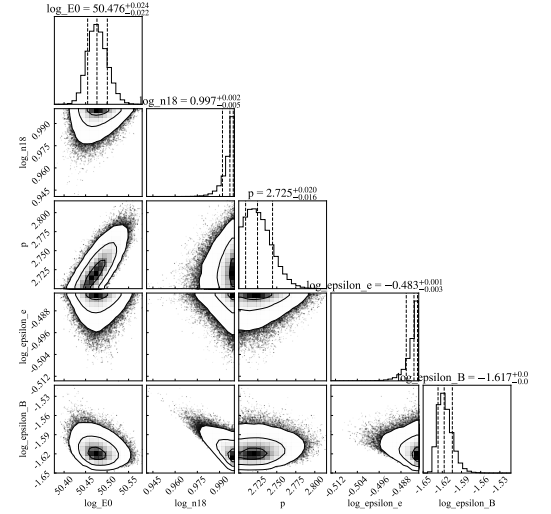
This value represents the outflowing mass required to supply the two-sided kinetic energy inferred from the radio afterglow, under the assumption that all of this kinetic energy is carried by material moving at $v = 0.03c$.

The outflow mass inferred above represents only the material that effectively participates in driving the forward shock. If the total disrupted mass associated with the second partial stripping event is denoted by M_2 , we have

$$\begin{aligned}
 M_2 &= \frac{2E_{\text{true}}}{\xi f_M v^2} \simeq 0.062 M_\odot \left(\frac{0.03c}{v} \right)^2 \\
 & \times \left(\frac{E_{\text{iso}}}{10^{50} \text{ erg}} \right) \left(\frac{1}{f_M} \right) \left(\frac{1}{\xi} \right).
 \end{aligned} \tag{9}$$



(a) Best-fit radio light curves of the late-time emission associated with the second flare.



(b) Posterior probability distributions from the MCMC fitting for the second radio flare.

Figure 3. Modeling results for the second radio flare of IGR J12580+0134. The left panel shows the best-fit radio light curves at 1.5, 3, and 6 GHz overlaid on the observational data from *E. S. Perlman et al. (2022)*, where the flux densities at 3 and 6 GHz are scaled down by factors of 10 and 10^2 for clarity. The right panel presents the posterior distributions of the synchrotron afterglow parameters derived from MCMC sampling.

where f_M is the fraction of the disrupted mass that is launched into the outflow, and ξ is the fraction of the outflow kinetic energy that is converted into the forward-shock energy inferred from radio modeling.

We note that the mass scale M_2 inferred from the radio afterglow energetics in this section characterizes the amount of material participating in the outflow/fallback during the second passage.

4. RESULTS AND DISCUSSION

4.1. Best-fit Modeling of the second Radio flare

To investigate the physical origin of the radio emission from IGR J12580+0134, we performed broadband afterglow modeling based on the standard GRB afterglow framework, utilizing the PyFRS² code (*W.-H. Lei et al. 2016; Z.-P. Zhu et al. 2023; C. Zhou et al. 2024; S.-Y. Fu et al. 2024*). The modeling was implemented using Markov Chain Monte Carlo (MCMC) techniques to constrain the relevant microphysical and dynamical parameters.

We adopted MJD 57340 as the zero-point for time calibration, corresponding to the presumed onset of the second radio flare. Due to the limited number of data points during this episode, we fixed several model parameters to reduce degeneracies in the fitting. Specifi-

cally, we assumed a uniform interstellar medium (ISM) environment, with the scale index of the ambient density profile fixed at $k = 0$, indicating a constant density environment. The outflow was assumed to be non-relativistic with a velocity of $v = 0.03c$, consistent with the expected expansion speed of a mildly energetic TDE ejecta.

Figure 3a shows the best-fit light curves at 1.5 GHz, 3 GHz, and 6 GHz, overplotted with the observed data points. Figure 3b is the corresponding corner plot of the posterior distributions. The model successfully reproduces the rise and decay features of the flare across all three bands. These results support the scenario where the radio flare is produced by the interaction between a mildly relativistic outflow and a dense ISM environment, consistent with expectations for TDEs in gas-rich galactic centers.

To validate the electron power-law index p obtained from the MCMC fitting, we performed an independent spectral analysis using multi-frequency data. Due to the limited availability of epochs with simultaneous observations in multiple bands, only two epochs contain measurements in the C, S, and L bands: 16 March 2016 and 21 May 2016, both taken under the VLA project 16A-420. However, the March 16 observation occurred during the rising phase of the radio flare and is therefore excluded from spectral fitting because of the departure from standard synchrotron assumptions.

² <https://github.com/leiwH/PyFRS>

In addition, we identified two closely spaced epochs between MJD 58000 and 59000 that provide S-band and L-band coverage. As shown in Table 2, these correspond to the S-band observation on 21 April 2019 (from the VLASS survey) and the L-band observation on 24 June 2019 (project 19A-425). Although these observations are separated by approximately two months, the radio flux is in a stable decay phase, well past the second flare which occurred over three years earlier. Therefore, we interpolated the L-band flux in the previous epoch (April 21, 2019), resulting in an estimated value of 62 mJy, as shown in Figure 4.

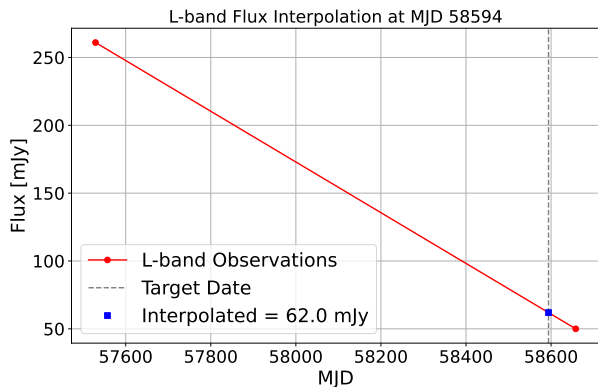


Figure 4. Linear interpolation of L-band flux at MJD 58594. Red circles denote the observed L-band flux densities at two epochs, and the blue square represents the interpolated value at the target date, yielding a flux of 62.0 mJy. The vertical dashed line marks the interpolation time. This value is used to reconstruct the broadband spectrum at a common epoch with the S-band measurement.

Using the spectral energy distributions (SEDs) obtained from the May 2016 data and the interpolated April 2019 data, we fitted the radio spectra with a power-law model in log–log space. A weighted least-squares minimization was employed to account for measurement uncertainties, yielding the synchrotron spectral index β , from which we derived the corresponding electron energy index. The fitting results and the SED plots are presented in Figure 5.

We emphasize that different formulas should be applied when converting the spectral index β to the electron energy index p , depending on the cooling regime of the afterglow. According to H. Gao et al. (2013), when the observed frequency lies between the characteristic synchrotron frequency ν_m and the cooling frequency ν_c (i.e., $\nu_m < \nu < \nu_c$), the appropriate relation is $p = 2\beta + 1$.

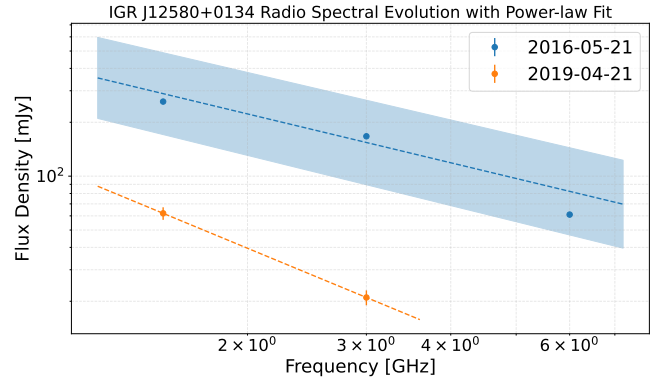


Figure 5. Radio spectral fits of IGR J12580+0134 at two different epochs: 2016-05-21 (blue) and 2019-04-21 (orange). The data points represent observed flux densities at multiple frequencies, while the dashed lines show the best-fit power-law models. The shaded regions indicate the 1σ confidence intervals propagated from the uncertainty in the spectral index β . The steeper slope observed in 2019 suggests a significant spectral evolution over the three-year period. Notably, the flux density decline between 3 and 6 GHz in the 2016 data appears steeper and closely matches the spectral slope of the 2019 epoch. This suggests that by 2016 May 21, the cooling frequency ν_c had likely decreased below 6 GHz, placing the observing band within the fast-cooling regime.

However, when the cooling frequency has dropped below the observing band ($\nu > \nu_c$), the fast cooling regime applies, and we adopt $p = 2\beta$.

In our case, the 2016-05-21 observation probably falls in the slow cooling regime, and we therefore use $p = 2\beta + 1$ for this epoch. For the 2019-04-21 data, the cooling frequency has probably decreased below the observing band, so we use $p = 2\beta$.

Using this reasoning, we derive the following values:

- **2016-05-21:** $\beta = 0.907 \pm 0.025 \Rightarrow p = 2.814 \pm 0.050$
- **2019-04-21:** $\beta = 1.562 \pm 0.180 \Rightarrow p = 3.124 \pm 0.360$

These results are consistent with the values of p inferred independently of the MCMC modeling, supporting the reliability of both the spectral fitting and the dynamical interpretation.

We note that our modeling of the second radio flare shares important similarities with the approach adopted by W.-H. Lei et al. (2016), while leading to a fundamentally different dynamical interpretation. In both studies, the radio emission is modeled within the standard GRB afterglow framework, where the synchrotron radiation arises from the interaction between an outflow and a circumnuclear medium. The broadband radio light curves

are interpreted using the same underlying synchrotron shock physics.

However, the dynamical properties inferred for the two episodes differ significantly. W.-H. Lei et al. (2016) and Q. Yuan et al. (2016) interpreted the early radio emission following the 2011 TDE as originating from an off-axis relativistic jet interacting with the surrounding medium. In their model, a relativistic outflow with an initial Lorentz factor $\Gamma_0 \gtrsim$ a few and a viewing angle $\theta_{\text{obs}} \gtrsim 30^\circ$ was required to simultaneously reproduce the radio light curves and satisfy the X-ray constraints.

In contrast, the second radio flare investigated here occurs approximately four years after the first event and is not accompanied by a luminous X-ray counterpart. Our MCMC modeling indicates that the radio emission can be consistently explained by a non-relativistic outflow with a characteristic velocity $v \approx 0.03c$ expanding into a uniform ISM environment. No strong beaming correction is required in this case.

This contrast suggests that the two flares may correspond to physically distinct dynamical phases. The first episode likely involved a relativistic jet launched during the initial disruption, whereas the second flare may instead trace a renewed, lower-energy outflow episode associated with a subsequent partial TDE.

4.2. Is dust extinction responsible for the optical faintness?

As shown in Figure 6, no significant optical variability is detected during the second radio flare, with all measurements remaining within the 3σ level. These data were obtained from the ASAS-SN survey, specifically in the V-band, which provides optical monitoring of transient events. From the observations we can compute an upper limit on the optical variability. The derived observed upper limit of $\nu L_\nu(V) \lesssim 1.4 \times 10^{41} \text{ erg s}^{-1}$. We estimate the dust extinction implied by the intrinsic hydrogen column density. Since no constraint on N_{H} is available for the second radio flare, we adopt the value derived from the 2023 X-ray flare for our extinction estimate. We estimate the optical extinction using the empirical relation $N_{\text{H}}/A_V \simeq 1.79 \times 10^{21} \text{ cm}^{-2} \text{ mag}^{-1}$ (P. Predehl & J. H. M. M. Schmitt 1995). For $N_{\text{H}} = 8 \times 10^{20} \text{ cm}^{-2}$ (A. Danehkar 2025), this gives $A_V \approx 0.45 \text{ mag}$. Assuming a standard Galactic extinction law (J. A. Cardelli et al. 1989) with $R_V = 3.1$, the inferred $A_V \approx 0.45 \text{ mag}$ implies that the extinction-corrected emission (or variability upper limit) in the ASAS-SN V band can be at most a factor of $10^{0.4A_V} \approx 1.51$ higher. Applying this correction increases from $\nu L_\nu(V) \lesssim 1.4 \times 10^{41}$ to $\nu L_\nu(V) \lesssim 2.1 \times 10^{41} \text{ erg s}^{-1}$. This modest correction indicates that dust extinction

cannot account for the optical faintness, suggesting that the weak optical emission during the second flare of IGR J12580+0134 is an intrinsic characteristic of the event.

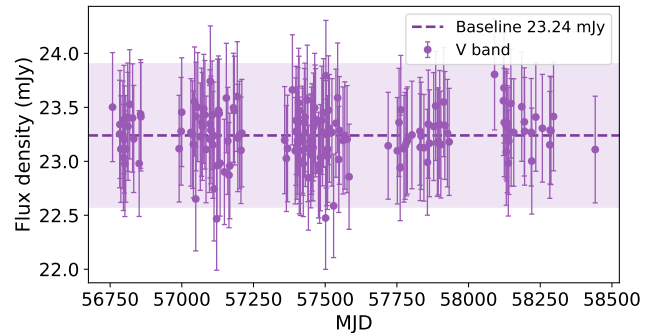


Figure 6. Optical light curve of IGR J12580+0134 in the ASAS-SN V band. The purple points show the ASAS-SN V-band flux density as a function of MJD. The dashed horizontal line indicates the weighted mean baseline flux ($F_0 = 23.24 \text{ mJy}$), and the shaded region represents the $\pm 3\sigma$ dispersion around this baseline. No significant optical variability beyond the 3σ level is detected during the second radio flare.

We note that the extinction estimate above is based on the column density measured during the 2023 X-ray flare ($N_{\text{H}} \simeq 8 \times 10^{20} \text{ cm}^{-2}$), which is nearly two orders of magnitude lower than the value reported for the first X-ray flare, $N_{\text{H}} \sim 7 \times 10^{22} \text{ cm}^{-2}$ (M. Nikolaĵuk & R. Walter 2013). As an illustrative scenario, if the line-of-sight column during the second radio flare were substantially higher than our fiducial value—e.g., $N_{\text{H}} \approx 7 \times 10^{21} \text{ cm}^{-2}$ —and if the gas-to-dust ratio were close to the Galactic value, the implied extinction would be $A_V \approx 3.9 \text{ mag}$, corresponding to a flux correction factor of ~ 36 . In this case, the extinction-corrected optical luminosity would increase to $\sim 5 \times 10^{42} \text{ erg s}^{-1}$, consistent with the faint end of optical TDEs. Such a low optical luminosity would be naturally explained if the disrupted object were less massive than in typical optically bright TDEs (S. van Velzen et al. 2020), although this inference remains model dependent.

4.3. Possible Explanations for the Lack of an X-ray Counterpart to the Second Flare

The lack of a statistically significant X-ray brightening during the second radio flare does not necessarily imply the absence of accretion activity. Swift/XRT observations obtained around the epoch of the radio rebrightening had limited photon counts, requiring the co-addition of multiple datasets to achieve an adequate signal-to-noise ratio. Consequently, an intrinsically faint

or short-lived X-ray episode may have remained undetected.

One plausible explanation is that the peak of the accretion-powered emission occurred prior to the available X-ray observations. In TDEs, X-ray radiation is generally expected to trace the fallback and early accretion phases, whereas radio emission typically arises from the delayed interaction between the outflow and the surrounding medium (M. J. Rees 1988). If the second partial disruption followed a similar evolutionary sequence, the onset of accretion could have preceded the observed rise of the radio flare, leaving the X-ray peak missed by sparse temporal coverage.

Obscuration may also play a secondary role. The first flare exhibited a heavily absorbed spectrum with a hydrogen column density of $N_{\text{H}} \sim 7 \times 10^{22} \text{cm}^{-2}$ (M. Niłojajuk & R. Walter 2013), demonstrating that substantial line-of-sight material can exist in this system while still allowing detectable hard X-ray emission. However, obscuration alone is unlikely to fully account for the non-detection unless the intrinsic luminosity of the second event was lower or its spectrum significantly softer than that of the 2011 outburst. A reduced fallback mass during the second encounter would naturally lead to a weaker accretion flow, consistent with the expectations for repeated partial tidal stripping.

An alternative possibility is that the second episode was dominated by kinetic energy carried by the outflow rather than by radiatively efficient accretion. In this scenario, the radio emission would primarily trace the shock interaction with a dense circumnuclear environment, while the high-energy signature could remain intrinsically faint (K. D. Alexander et al. 2020). Such behavior has been suggested in several low-luminosity or inefficiently accreting TDEs.

Overall, the current data do not strongly discriminate between an intrinsically weak X-ray flare, incomplete temporal coverage, or moderate obscuration. Deeper and higher-cadence X-ray monitoring will be essential for determining whether future passages produce detectable high-energy counterparts, thereby clarifying the accretion properties of this candidate repeating partial tidal disruption system.

5. SUMMARY

We present a multi-wavelength study of IGR J12580+0134 in NGC 4845, motivated by the late-time radio rebrightening reported several years after the 2011 X-ray tidal-disruption flare (M. Niłojajuk & R. Walter 2013; J. A. Irwin et al. 2015; E. S. Perlman et al. 2022). We compile the available radio and X-ray measurements

and model the second radio flare within a standard synchrotron afterglow framework.

Our radio modeling constrains the outflow energetics and ambient density associated with the 2016 episode, indicating a mildly energetic, non-relativistic ejecta interacting with a dense circumnuclear environment. The inferred energetics imply that only a modest amount of mass is required to power the radio emission, consistent with a partial mass-loss episode rather than a single complete disruption. In this context, the comparatively low disrupted mass inferred for the 2011 event can be interpreted as the stripped mass that entered fallback and accretion, rather than the total mass of the disrupted object (M. Niłojajuk & R. Walter 2013; W.-H. Lei et al. 2016).

On the high-energy side, Swift/XRT observations obtained during the 2016 radio flare did not show a statistically significant X-ray brightening (E. S. Perlman et al. 2022). More recently, NICER monitoring revealed faint X-ray flares during March–June 2023 that are substantially weaker than the 2011 outburst, suggesting intermittent low-level accretion activity in the nucleus (A. Danehkar 2025).

Taken together, our results support a scenario in which IGR J12580+0134 is a promising candidate for a repeating pTDE. Future high-cadence, sensitive X-ray monitoring and continued radio follow-up will be essential for testing this interpretation and for searching for additional episodes on multi-year timescales.

ACKNOWLEDGMENTS

We thank the participants of the TDE FORUM (Full-process Orbital to Radiative Unified Modeling) online seminar series for their inspiring discussions. We are very grateful to Rongfeng Shen, Erlin Qiao, and Chichuan Jin for their helpful discussions. This work is supported by the National Key R&D Program of China (No. 2023YFC2205901) and the National Natural Science Foundation of China under grants 12473012, 12533005, and 12321003. This work is supported by Project for Young Scientists in Basic Research of Chinese Academy of Sciences (No. YSBR-061). W.H.Lei acknowledges support by the science research grants from the China Manned Space Project with NO.CMS-CSST-2021-B11.

Table 1. List of published repeated pTDE candidates

Name	Host Type	Band	Period/Interval (Days)	Flares	Peak Evolution
ASASSN-14ko ^{1,2,3,4,5}	Seyfert 2	Opt./UV/X-ray [†]	115.2	~30	Similar
Swift J023017.0+283603 ^{6,7}	Weak AGN	X-ray	~22	~11	Variable
eRASSt J045650.3–203750 ⁸	Quiescent	X-ray/UV [†]	299→193	5	Lower
AT 2023uqm ⁹	Quiescent	Opt./UV/X-ray [‡]	~527	≥5	Increasing
IC 3599 ^{10,11,12,13,14}	Seyfert 1.9	X-ray/Opt.*	~3470*	2/3	Similar
RX J133157.6–324319.7 ^{15,16}	Quiescent	X-ray	~10 000	2	Similar
AT 2018fyk ^{17,18,19}	Quiescent	UV/X-ray	~1200	2	Lower
AT 2019aalc ²⁰	Seyfert 1	Opt./UV/X-ray*	~1460	2	similar
AT 2020vdq ^{21,22}	E+A	Opt./UV*/X-ray*	~870	2	Higher
AT 2021aeuk ²³	Seyfert 1	Opt./UV/X-ray*	~1100	2	Variable
AT 2022dbl ^{24,25,26,27}	QBS	Opt./UV	~710	2	Lower
F01004-2237 ²⁸	Dusty starburst	Opt./UV/X-ray*	~3760	2	Lower
AT 2023adr ²⁹	Quiescent	Opt./UV	~ 420	2	Similar
AT 2022sxl ³⁰	Composite	Opt./MIR	~ 2600	2	Similar
AT 2019azh ³¹	E+A	Opt.	~ 4800	2	Similar
AT 2024pvu ³¹	Green valley	Opt./UV	~ 6200	2	Similar

NOTE—

[†] Not periodic.

* Not observed during the first flare.

[‡] X-ray observations were obtained only during the fifth flare.* IC 3599 exhibited two prominent X-ray flares in 1990 and 2010. Based on a repeated pTDE interpretation, [S. Campana et al. \(2015\)](#) proposed a recurrence period of ~9.5 yr, implying a missed flare between the two events. However, subsequent X-ray monitoring did not detect an additional flare within the predicted time window ([D. Grupe et al. 2024](#)).References: 1. [A. V. Payne et al. \(2021\)](#), 2. [A. V. Payne et al. \(2022\)](#), 3. [A. V. Payne et al. \(2023\)](#), 4. [S. Huang et al. \(2023\)](#), 5. [A. Bandopadhyay et al. \(2024\)](#), 6. [P. A. Evans et al. \(2023\)](#), 7. [M. Guolo et al. \(2024\)](#), 8. [Z. Liu et al. \(2024\)](#), 9. [Y. Wang et al. \(2025\)](#), 10. [D. Grupe et al. \(1995\)](#), 11. [S. Komossa & N. Bade \(1999\)](#), 12. [D. Grupe et al. \(2015\)](#), 13. [S. Campana et al. \(2015\)](#), 14. [D. Grupe et al. \(2024\)](#), 15. [J. Hampel et al. \(2022\)](#), 16. [A. Malyali et al. \(2023\)](#), 17. [T. Wevers et al. \(2019\)](#), 18. [T. Wevers et al. \(2023\)](#), 19. [D. Pasham et al. \(2024\)](#), 20. [P. M. Veres et al. \(2025\)](#), 21. [Y. Yao et al. \(2023\)](#), 22. [J. J. Somalwar et al. \(2025\)](#), 23. [J. Sun et al. \(2025\)](#), 24. [Y. Yao et al. \(2024\)](#), 25. [Z. Lin et al. \(2024\)](#) 26. [J. T. Hinkle et al. \(2025\)](#), 27. [L. Makrygianni et al. \(2025\)](#) 28. [L. Sun et al. \(2024\)](#) 29. [C. R. Angus et al. \(2026\)](#) 30. [S. Ji et al. \(2025\)](#) 31. [Y. Yao et al. \(2026\)](#)

Table 2. VLA Observations

Date ^a	Project ^b	ΔT^c (days)	Config ^d	Freq ^e (Band) (GHz)	ΔB^f (MHz)	Beam ^g (u, v, ϕ)	RMS ^h (mJy/beam)	Nuclear Flux ⁱ Density (mJy)
1995-Feb-27	NVSS ^j	-6150	D	1.4 (L)	50	45, 45, 0	0.45	26 ± 4
1998-Jul-26	AB0879 ^k	-4905	B	1.4 (L)	100	5.1, 4.2, 24.0	1.0	34 ± 2
2011-Dec-19	10C-119 ^l	-11	D	6.0 (C)	2048	11.0, 9.1, -1.4	0.015	425 ± 3
2011-Dec-30 (T1)	10C-119 ^l	0	D	1.6 (L)	500	38.6, 34.3, -5.22	0.040	211 ± 3
2012-Feb-24	10C-119 ^l	56	C	6.0 (C)	2048	3.1, 2.8, -11.7	0.0039	355 ± 2
2012-Mar-30	10C-119 ^l	91	C	1.6 (L)	500	12.2, 11.1, -41.8	0.045	241 ± 3
2012-Jun-11	10C-119 ^l	164	B	1.6 (L)	500	3.5, 3.3, 22.7	0.018	219 ± 4
2015-Jun-22	15A-357 ^m	1270	A	1.5 (L)	1000	1.73, 1.06, 43.2	0.12	115 ± 2
2015-Jun-22	15A-357 ^m	1270	A	5.5 (C)	1000	0.47, 0.33, 46.2	0.013	36.3 ± 0.3
2015-Jul-06	15A-400 ^k	1284	A	9 (X)	2048	0.21, 0.2, 20	0.010	22.7 ± 0.3
2015-Jul-14	15A-400 ^k	1292	A	9 (X)	2048	0.27, 0.16, 43	0.020	17.1 ± 0.2
2015-Jul-28	15A-400 ^k	1306	A	6 (C)	2048	0.37, 0.28, 48.5	0.015	33.6 ± 0.2
2016-Mar-16	16A-420 ^k	1538	C	6.0 (C)	2048	3.5, 3.0, -52.5	0.012	27 ± 2
2016-Mar-16	16A-420 ^k	1538	C	3.0 (S)	2048	6.4, 5.2, -18.4	0.032	60 ± 3
2016-Mar-16	16A-420 ^k	1538	C	1.5 (L)	1024	12.9, 9.9, -21.0	0.48	171 ± 5
2016-May-21	16A-420 ^k	1604	B	6.0 (C)	2048	0.98, 0.86, -23.5	0.034	61 ± 2
2016-May-21	16A-420 ^k	1604	B	3.0 (S)	2048	1.8, 1.7, -20.0	0.058	167 ± 2
2016-May-21	16A-420 ^k	1604	B	1.5 (L)	1024	3.6, 3.1, -20.7	0.50	261 ± 5
2019-Apr-21	VCLASS ^k	2669	B	3.0 (S)	2048	2.9, 2.1, 31.1	0.169	21 ± 2
2019-Jun-24	19A-425 ^k	2733	B	1.5 (L)	64	4.9, 3.3, -13.8	0.170	50 ± 5
2021-Sep-14	21A-033 ⁿ	3546	C→B	3.0 (S)	2048	2.92, 1.39, -2.83	0.110	9.53 ± 1
2022-Oct-08	22B-016 ⁿ	3935	C	3.0 (S)	2048	6.55, 5.07, 42.67	0.04	19.97 ± 1
2024-Jun-25	VCLASS ^o	4561	B	3.0 (S)	2048	3.19, 2.13, 36.00	0.16	13.8 ± 4

^a Date of observation.

^b Project name or code.

^c Elapsed time since T1 = Dec 30, 2011.

^d VLA array configuration.

^e Central frequency of the band followed by the name of the band in parentheses.

^f Total bandwidth.

^g Synthesized beam major axis, minor axis, and position angle.

^h Measured rms map noise (primary beam corrected, near source).

ⁱ Flux of nucleus after correction for surrounding disk emission for low resolution images.

^j Downloaded and measured from the NRAO VLA Sky Survey (NVSS, J. J. Condon et al. 1998)

^k Data from E. S. Perlman et al. (2022)

^l Data from J. A. Irwin et al. (2015).

^m Data from E. S. Perlman et al. (2017).

ⁿ This work.

^o This work. Measured from VCLASS data (VCLASS; M. Lacy et al. 2020), download form <https://archive-new.nrao.edu/vlass/quicklook/>

REFERENCES

- Alexander, K. D., van Velzen, S., Horesh, A., & Zauderer, B. A. 2020, *Space Science Reviews*, 216, 81
- Angus, C. R., Smith, A. J., Magill, D., et al. 2026, <https://arxiv.org/abs/2601.04406>
- Arcavi, I., Gal-Yam, A., Sullivan, M., et al. 2014, *ApJ*, 793, 38, doi: [10.1088/0004-637X/793/1/38](https://doi.org/10.1088/0004-637X/793/1/38)
- Bandopadhyay, A., Coughlin, E. R., Nixon, C., & Pasham, D. R. 2024, *The Astrophysical Journal*, 974, 80
- Campana, S., Mainetti, D., Colpi, M., et al. 2015, *A&A*, 581, A17, doi: [10.1051/0004-6361/201525965](https://doi.org/10.1051/0004-6361/201525965)
- Cardelli, J. A., Clayton, G. C., & Mathis, J. S. 1989, *ApJ*, 345, 245, doi: [10.1086/167900](https://doi.org/10.1086/167900)
- Chen, J.-H., & Shen, R.-F. 2021, *ApJ*, 914, 69, doi: [10.3847/1538-4357/abf9a7](https://doi.org/10.3847/1538-4357/abf9a7)
- Chen, J.-H., Shen, R.-F., & Liu, S.-F. 2023, *ApJ*, 947, 32, doi: [10.3847/1538-4357/acfbf6](https://doi.org/10.3847/1538-4357/acfbf6)
- Clark, B. 1980, *Astronomy and Astrophysics*, vol. 89, no. 3, Sept. 1980, p. 377, 378., 89, 377
- Condon, J. J., Cotton, W., Greisen, E., et al. 1998, *The Astronomical Journal*, 115, 1693
- Coughlin, E. R., & Nixon, C. J. 2019, *The Astrophysical Journal Letters*, 883, L17, doi: [10.3847/2041-8213/ab412d](https://doi.org/10.3847/2041-8213/ab412d)
- Coughlin, E. R., & Nixon, C. J. 2022, *Monthly Notices of the Royal Astronomical Society: Letters*, 517, L26, doi: [10.1093/mnrasl/slac106](https://doi.org/10.1093/mnrasl/slac106)
- Cufari, M., Coughlin, E. R., & Nixon, C. 2022, *The Astrophysical Journal Letters*, 929, L20
- Danehkar, A. 2025, *The Astrophysical Journal*, 986, 50, doi: [10.3847/1538-4357/adce7e](https://doi.org/10.3847/1538-4357/adce7e)
- Evans, P. A., Nixon, C. J., Campana, S., et al. 2023, *Nature Astronomy*, 7, 1368, doi: [10.1038/s41550-023-02073-y](https://doi.org/10.1038/s41550-023-02073-y)
- Ferrarese, L., & Merritt, D. 2000, *ApJL*, 539, L9, doi: [10.1086/312838](https://doi.org/10.1086/312838)
- Fu, S.-Y., Xu, D., Lei, W.-H., et al. 2024, *ApJ*, 977, 197, doi: [10.3847/1538-4357/ad8886](https://doi.org/10.3847/1538-4357/ad8886)
- Gao, H., Lei, W.-H., Zou, Y.-C., Wu, X.-F., & Zhang, B. 2013, *New Astronomy Reviews*, 57, 141
- Gebhardt, K., Bender, R., Bower, G., et al. 2000, *ApJL*, 539, L13, doi: [10.1086/312840](https://doi.org/10.1086/312840)
- Grupe, D., Beuermann, K., Mannheim, K., et al. 1995, *A&A*, 299, L5, doi: [10.48550/arXiv.astro-ph/9505085](https://doi.org/10.48550/arXiv.astro-ph/9505085)
- Grupe, D., Komossa, S., & Saxton, R. 2015, *ApJL*, 803, L28, doi: [10.1088/2041-8205/803/2/L28](https://doi.org/10.1088/2041-8205/803/2/L28)
- Grupe, D., Komossa, S., & Wolsing, S. 2024, *ApJ*, 969, 98, doi: [10.3847/1538-4357/ad4530](https://doi.org/10.3847/1538-4357/ad4530)
- Guillochon, J., & Ramirez-Ruiz, E. 2013, *The Astrophysical Journal*, 767, 25, doi: [10.1088/0004-637X/767/1/25](https://doi.org/10.1088/0004-637X/767/1/25)
- Guolo, M., Pasham, D. R., Zajaček, M., et al. 2024, *Nature Astronomy*, 8, 347, doi: [10.1038/s41550-023-02178-4](https://doi.org/10.1038/s41550-023-02178-4)
- Hammerstein, E., van Velzen, S., Gezari, S., et al. 2023, *ApJ*, 942, 9, doi: [10.3847/1538-4357/aca283](https://doi.org/10.3847/1538-4357/aca283)
- Hampel, J., Komossa, S., Greiner, J., et al. 2022, *Research in Astronomy and Astrophysics*, 22, 055004, doi: [10.1088/1674-4527/ac5800](https://doi.org/10.1088/1674-4527/ac5800)
- Hills, J. G. 1988, *Nature*, 331, 687
- Hinkle, J. T., Auchettl, K., Hoogendam, W. B., et al. 2025, <https://arxiv.org/abs/2412.15326>
- Huang, S., Jiang, N., Shen, R.-F., Wang, T., & Sheng, Z. 2023, *ApJL*, 956, L46, doi: [10.3847/2041-8213/acffc5](https://doi.org/10.3847/2041-8213/acffc5)
- Irwin, J., Krause, M., English, J., et al. 2013, *The Astronomical Journal*, 146, 164, doi: [10.1088/0004-6256/146/6/164](https://doi.org/10.1088/0004-6256/146/6/164)
- Irwin, J. A., Henriksen, R. N., Krause, M., et al. 2015, *ApJ*, 809, 172, doi: [10.1088/0004-637X/809/2/172](https://doi.org/10.1088/0004-637X/809/2/172)
- Irwin, J. A., Beck, R., Benjamin, R. A., et al. 2012, *The Astronomical Journal*, 144, 43, doi: [10.1088/0004-6256/144/2/43](https://doi.org/10.1088/0004-6256/144/2/43)
- Ji, S., Wang, Z., Zhu, L., Geier, S., & Gupta, A. C. 2025, <https://arxiv.org/abs/2508.09408>
- Komossa, S., & Bade, N. 1999, *A&A*, 343, 775, doi: [10.48550/arXiv.astro-ph/9901141](https://doi.org/10.48550/arXiv.astro-ph/9901141)
- Lacy, M., Baum, S. A., Chandler, C. J., et al. 2020, *Publications of the Astronomical Society of the Pacific*, 132, 035001, doi: [10.1088/1538-3873/ab63eb](https://doi.org/10.1088/1538-3873/ab63eb)
- Lei, W.-H., Yuan, Q., Zhang, B., & Wang, D. 2016, *The Astrophysical Journal*, 816, 20, doi: [10.3847/0004-637X/816/1/20](https://doi.org/10.3847/0004-637X/816/1/20)
- Li, D., Zhang, W., Yang, J., et al. 2025, *arXiv e-prints*, arXiv:2509.25877, doi: [10.48550/arXiv.2509.25877](https://doi.org/10.48550/arXiv.2509.25877)
- Lin, Z., Jiang, N., Wang, T., et al. 2024, *The Astrophysical Journal Letters*, 971, L26, doi: [10.3847/2041-8213/ad638e](https://doi.org/10.3847/2041-8213/ad638e)
- Liu, Z., Ryu, T., Goodwin, A. J., et al. 2024, *A&A*, 683, L13, doi: [10.1051/0004-6361/202348682](https://doi.org/10.1051/0004-6361/202348682)
- Lu, W., & Quataert, E. 2023, *MNRAS*, 524, 6247, doi: [10.1093/mnras/stad2203](https://doi.org/10.1093/mnras/stad2203)
- Makarov, D., Prugniel, P., Terekhova, N., Courtois, H., & Vaughn, I. 2014, *A&A*, 570, A13, doi: [10.1051/0004-6361/201423496](https://doi.org/10.1051/0004-6361/201423496)
- Makrygianni, L., Arcavi, I., Newsome, M., et al. 2025, <https://arxiv.org/abs/2505.16867>
- Malyali, A., Liu, Z., Rau, A., et al. 2023, *MNRAS*, 520, 3549, doi: [10.1093/mnras/stad022](https://doi.org/10.1093/mnras/stad022)
- Mandel, I., & Levin, Y. 2015, *The Astrophysical Journal*, 805, L4, doi: [10.1088/2041-8205/805/1/L4](https://doi.org/10.1088/2041-8205/805/1/L4)
- McConnell, N. J., & Ma, C.-P. 2013, *The Astrophysical Journal*, 764, 184, doi: [10.1088/0004-637X/764/2/184](https://doi.org/10.1088/0004-637X/764/2/184)

- McMullin, J. P., Waters, B., Schiebel, D., Young, W., & Golap, K. 2007, in ASP Conference Series, Vol. 376, *Astronomical Data Analysis Software and Systems XVI (ADASS XVI)*, ed. R. A. Shaw, F. Hill, & D. J. Bell (Astronomical Society of the Pacific), 127
- Nikołajuk, M., & Walter, R. 2013, *Astronomy & Astrophysics*, 552, A75
- Pasham, D., Coughlin, E., Guolo, M., et al. 2024, <https://arxiv.org/abs/2406.18124>
- Payne, A. V., Shappee, B. J., Hinkle, J. T., et al. 2021, *The Astrophysical Journal*, 910, 125
- Payne, A. V., Shappee, B. J., Hinkle, J. T., et al. 2022, *ApJ*, 926, 142, doi: [10.3847/1538-4357/ac480c](https://doi.org/10.3847/1538-4357/ac480c)
- Payne, A. V., Auchettl, K., Shappee, B. J., et al. 2023, *ApJ*, 951, 134, doi: [10.3847/1538-4357/acd455](https://doi.org/10.3847/1538-4357/acd455)
- Perley, R. A., & Butler, B. J. 2013, *The Astrophysical Journal Supplement Series*, 204, 19, doi: [10.1088/0067-0049/204/2/19](https://doi.org/10.1088/0067-0049/204/2/19)
- Perlman, E. S., Meyer, E. T., Wang, Q. D., et al. 2017, *The Astrophysical Journal*, 842, 126
- Perlman, E. S., Meyer, E. T., Wang, Q. D., et al. 2022, *The Astrophysical Journal*, 925, 143, doi: [10.3847/1538-4357/ac3bba](https://doi.org/10.3847/1538-4357/ac3bba)
- Pfister, H., Volonteri, M., Dai, J. L., & Colpi, M. 2020, *MNRAS*, 497, 2276, doi: [10.1093/mnras/staa1962](https://doi.org/10.1093/mnras/staa1962)
- Phinney, E. 1989, in *Symposium-International Astronomical Union*, Vol. 136, Cambridge University Press, 543–553
- Predehl, P., & Schmitt, J. H. M. M. 1995, *A&A*, 293, 889
- Quinlan, G. D. 1996, *New Astronomy*, 1, 35, doi: [https://doi.org/10.1016/S1384-1076\(96\)00003-6](https://doi.org/10.1016/S1384-1076(96)00003-6)
- Rau, U., & Cornwell, T. J. 2011, *Astronomy & Astrophysics*, 532, A71
- Rees, M. J. 1988, *Nature*, 333, 523
- Ryu, T., Krolik, J., Piran, T., & Noble, S. C. 2020a, *The Astrophysical Journal*, 904, 100, doi: [10.3847/1538-4357/abb3ce](https://doi.org/10.3847/1538-4357/abb3ce)
- Ryu, T., Krolik, J., Piran, T., & Noble, S. C. 2020b, *The Astrophysical Journal*, 904, 100
- Shen, R.-F. 2019, *ApJL*, 871, L17, doi: [10.3847/2041-8213/aafc64](https://doi.org/10.3847/2041-8213/aafc64)
- Somalwar, J. J., Ravi, V., Yao, Y., et al. 2025, *ApJ*, 985, 175, doi: [10.3847/1538-4357/adcc19](https://doi.org/10.3847/1538-4357/adcc19)
- Stone, N. C., & Metzger, B. D. 2016, *MNRAS*, 455, 859, doi: [10.1093/mnras/stv2281](https://doi.org/10.1093/mnras/stv2281)
- Stone, N. C., Vasiliev, E., Kesden, M., et al. 2020, *Space Science Reviews*, 216, 35, doi: [10.1007/s11214-020-00651-4](https://doi.org/10.1007/s11214-020-00651-4)
- Sun, J., Guo, H., Gu, M., et al. 2025, arXiv preprint arXiv:2501.01824
- Sun, L., Jiang, N., Dou, L., et al. 2024, *Astronomy & Astrophysics*, 692, A262, doi: [10.1051/0004-6361/202452380](https://doi.org/10.1051/0004-6361/202452380)
- van Velzen, S., Holoien, T. W.-S., Onori, F., Hung, T., & Arcavi, I. 2020, *SSRv*, 216, 124, doi: [10.1007/s11214-020-00753-z](https://doi.org/10.1007/s11214-020-00753-z)
- Veres, P. M., Franckowiak, A., van Velzen, S., et al. 2025, <https://arxiv.org/abs/2408.17419>
- Walter, R., Bordas, P., Bozzo, E., et al. 2011, *The Astronomer's Telegram*, 3108, 1
- Wang, M., Ma, Y., Wu, Q., & Jiang, N. 2024, *ApJ*, 960, 69, doi: [10.3847/1538-4357/ad0bfb](https://doi.org/10.3847/1538-4357/ad0bfb)
- Wang, Y., Lin, Z., Wu, L., et al. 2025, *Science Advances*, 11, 25.9068, doi: [10.1126/sciadv.ady9068](https://doi.org/10.1126/sciadv.ady9068)
- Wang, Y., Wang, T., Huang, S., et al. 2025, <https://arxiv.org/abs/2510.26561>
- Wevers, T., Pasham, D. R., van Velzen, S., et al. 2019, *MNRAS*, 488, 4816, doi: [10.1093/mnras/stz1976](https://doi.org/10.1093/mnras/stz1976)
- Wevers, T., Coughlin, E. R., Pasham, D. R., et al. 2023, *ApJL*, 942, L33, doi: [10.3847/2041-8213/ac9f36](https://doi.org/10.3847/2041-8213/ac9f36)
- Wiegert, T., Irwin, J., Miskolczi, A., et al. 2015, *The Astronomical Journal*, 150, 81, doi: [10.1088/0004-6256/150/3/81](https://doi.org/10.1088/0004-6256/150/3/81)
- Wu, X.-J., & Yuan, Y.-F. 2018, *MNRAS*, 479, 1569, doi: [10.1093/mnras/sty1423](https://doi.org/10.1093/mnras/sty1423)
- Yao, Y., Chornock, R., LeBaron, N., et al. 2024, *Transient Name Server AstroNote*, 43, 1
- Yao, Y., Sun, L., Wu, T., et al. 2026, <https://arxiv.org/abs/2601.12691>
- Yao, Y., Ravi, V., Gezari, S., et al. 2023, *ApJL*, 955, L6, doi: [10.3847/2041-8213/acf216](https://doi.org/10.3847/2041-8213/acf216)
- Yu, N., Ho, L. C., Wang, J., & Li, H. 2022, *ApJS*, 261, 21, doi: [10.3847/1538-4365/ac626b](https://doi.org/10.3847/1538-4365/ac626b)
- Yuan, Q., Wang, Q. D., Lei, W.-H., Gao, H., & Zhang, B. 2016, *Monthly Notices of the Royal Astronomical Society*, 461, 3375
- Zhong, S., Li, S., Berczik, P., & Spurzem, R. 2022, *ApJ*, 933, 96, doi: [10.3847/1538-4357/ac71ad](https://doi.org/10.3847/1538-4357/ac71ad)
- Zhou, C., Zhu, Z.-P., Lei, W.-H., et al. 2024, *ApJ*, 963, 66, doi: [10.3847/1538-4357/ad20f3](https://doi.org/10.3847/1538-4357/ad20f3)
- Zhu, Z.-P., Xu, D., Fynbo, J. P. U., et al. 2023, *ApJ*, 948, 30, doi: [10.3847/1538-4357/acbd96](https://doi.org/10.3847/1538-4357/acbd96)